

---

# Visualizing LSTM decisions

---

Jos van der Westhuizen

Joan Lasenby

University of Cambridge  
{jv365, j1221}@cam.ac.uk

## Abstract

Long Short-Term Memory (LSTM) recurrent neural networks are renowned for being uninterpretable "black boxes". In the medical domain where LSTMs have shown promise, this is specifically concerning because it is imperative to understand the decisions made by machine learning models in such acute situations. This study employs techniques used in the Convolutional Neural Network domain to elucidate the operations that LSTMs perform on time series. The visualization techniques include input saliency by means of occlusion and derivatives, class mode visualization, and temporal outputs. Moreover, we demonstrate that LSTMs appear to extract features similar to those extracted by wavelets. It was found that deriving the inputs for saliency is a poor approximation and occlusion is a better approach. Moreover, analyzing LSTMs on different sets of data provide novel interpretations.

## 1 Introduction

Deep learning has led to groundbreaking results in multiple fields such as natural language processing [24], computer vision [11], and computational biology [30, 12]. In the medical domain, it is imperative for doctors and researchers that use these models to understand how the models make predictions or classifications. Thus elucidating what the "black box" models do during analysis is a key step towards enabling a greater understanding in their practical use.

One class of deep learning models that has shown the most promise for temporal data in medicine is Long Short-Term Memory (LSTM) Recurrent Neural Networks (RNNs) [6, 16, 17, 7]. The core challenge of LSTMs is understanding what these complex models pay attention to when classifying signals, and what operations are applied to the time series during analysis. Convolutional Neural Networks (CNNs) have witnessed fundamental insights into their operation by visualizing the filters that are applied through methods such as deconvolution of the output and visualizing the saliency projected onto the input image [28, 23]. However, LSTMs arguably perform more complex operations on the data, which are less interpretable than those in CNNs.

Previous work on the understanding and visualization of RNNs have made admirable advances toward a better understanding of what operations RNNs perform on the data [9, 14]. These studies approach the problem from a natural language processing perspective and elucidate the RNN analysis in the form of grids. A problem with such approaches is that they aren't intuitive from the classical signal processing perspective.

Our approach is to find a signal processing intuition for the analysis performed by LSTMs with a specific focus on interpretability for the medical field. This is achieved by (i) demonstrating that the first layer of an LSTM learns filters such as the wavelet transform to extract features from signals, and (ii) depicting what LSTMs focus on when analyzing time series by means of first derivatives, class mode visualization, sequence propagation, and occlusion filters.

Elucidating that trained models perform similar operations to conventional filtering techniques, such as the wavelet transformation, supports the argument that serendipitous discovery of important

features leads to improved results. In the image processing domain, it was starkly shown that for the current state of machine learning, learning end-to-end (without hand-engineering features) results in the best performance [11]. In medicine, where accuracy is paramount, learning end-to-end is also the superior approach and knowing that the learned models perform operations similar to hand-engineered approaches can reinforce the confidence of medical practitioners in the recent "black box" approaches. Moreover, adroit application of the saliency detection methods discussed in this work, allows medical practitioners to understand what inputs the LSTMs focus on, and where they could possibly fail in medical diagnostics.

## 2 Related work

Deep Neural Network (DNN) visualization techniques have been explored in other domains. Li et al. [14] visualized RNN embedding vectors to show how RNNs achieve compositionality in natural language for sentiment analysis as well as visualizing the influence of input words on classification. Karpathy et al. [9] analyzed the interpretability of RNNs for language modeling, demonstrating the existence of interpretable neurons which are able to focus on specific language structures such as quotation marks in text. Lanchantin et al. [12] explored inference of important local sequences of DNA for classification based on what is salient for the DNN models. In both the text-based studies, the aim was to improve the understanding of LSTMs based on knowledge of the structured language. In the DNA-based study, as with medicine in general, we are uncertain about the underlying biological processes and DNNs can play a vital role in illuminating new assertions. The aim of our work is to contribute both to a better understanding of the important underlying biological processes when making medical predictions and to broaden the understanding of LSTMs by means of a different type of dataset.

The extraction of frequency domain features is imperative in signal processing. The Fourier transform is the core of frequency analysis, but it is a poor descriptor due to the infinite support of its basis functions. The Wavelet transform, like the Fourier transform, can be used to decompose a signal into its frequency components. The Wavelet transform provides full flexibility on the spatial or frequency resolution required and is in most cases a superior solution to the Fourier transform. Multiple studies have combined wavelets and Neural Networks. Li et al. [15] combined LSTMs with wavelet coefficients to yield improved classification performance. Jiang and Adeli [8] proposed a novel time-delay recurrent wavelet neural network model to forecast traffic flow. The model is not recurrent in the NN sense, but rather the output is recurrently fed into new wavelets. Wavelets have been used for feature extraction to serve as input to Neural Networks that aim to classify Phonocardiogram recordings [27]. Gal [3] demonstrated that NNs can be viewed as a the Fourier expansion with the Fourier frequencies and coefficients representing specific NN parameters.

## 3 Experimental setup

To demonstrate the utility of the proposed techniques, we made use of 4 datasets; the MNIST dataset [13] processed in scanline order [2], the MIT-BIH Arrhythmia dataset [18, 4] of electrocardiogram (ECG) signals, a 3-class multivariate (ECG, blood pressure (BP), oxygen saturation) dataset of 3 patients from a neonatal intensive care unit (NICU), and a 2-class multivariate (ECG, BP, intracranial pressure) dataset of 4 patients in a intensive care unit (ICU). Additional details about the datasets are provided in the supplementary material. Each dataset made use of the same model with a different architecture. The models were trained using Adam [10], a dropout probability of 0.2, a minibatch size of 256, and a learning rate of 0.001. All datasets were randomly split with a ratio of 50:40:10 (train:test:validation), except for the MNIST dataset which was provided with a random split.

The LSTM employed is based on [7] and is implemented in Tensorflow [1]. The outputs of the final LSTM layer are linearly mapped into the output dimension. The resulting matrix is average pooled over time before being subjected to a softmax function. Validation data was used to determine the optimal model parameters. Table 1 summarizes the accuracies obtained by the models analyzed in this study (average accuracies for 10 trials). Our model performance on the ECG dataset is similar to that in Oresko et al. [20] (0.98 weighted average accuracy over all 5 heart beat classes). Moreover, the accuracy obtained for the MNIST dataset is the same as the results reported in Cooijmans et al. [2] and Zhang et al. [29] (0.989 and 0.981 respectively).

Table 1: Experiment Accuracies

Dataset	Hidden units per layer	Accuracy
MNIST	128x128	0.987
MIT-BIH	128	0.985
NICU	64	0.997
ICU	128	0.982

## 4 LSTMs as filters

Traditionally, machine learning techniques were coupled with hand-engineered features on various learning tasks. The work by Krizhevsky et al. [11] demonstrated that learning from the data in an end-to-end fashion with a model that has sufficient descriptive capacity, yields a better performance compared to hand-engineered approaches. Zeiler and Fergus [28] followed this work to show that the large models trained end-to-end learn filters similar to those that would have been hand-engineered. These advances have mostly been restricted to the image processing and CNN field, and machine learning in medicine still prefers the hand-engineered approach [26, 21, 27].

There are various internal mechanisms of the LSTM that when analyzed could elucidate the internal operations performed when processing a signal for classification. These mechanisms include the input, output and forget gates (illustrated as their percentage of time spent close to one or close to zero in Karpathy et al. [9]); the hidden unit memory values  $c$  and output values  $h$ , and the input weights  $W$  and hidden unit weights  $U$  for each gate.

In CNNs the first layer of weights can be plotted to illustrate interpretable filters. Naive plotting of the weights in the LSTM for the implemented datasets did not elucidate any interpretable aspects of the model as exemplified by Figure 1 (left). Karpathy et al. [9] demonstrated that the hidden unit memories  $c$  have interpretable values when analyzing text. However, when processing medical signals such as ECG beats, the memory units in our LSTMs display uninterpretable values as shown in Figure 1 (right).

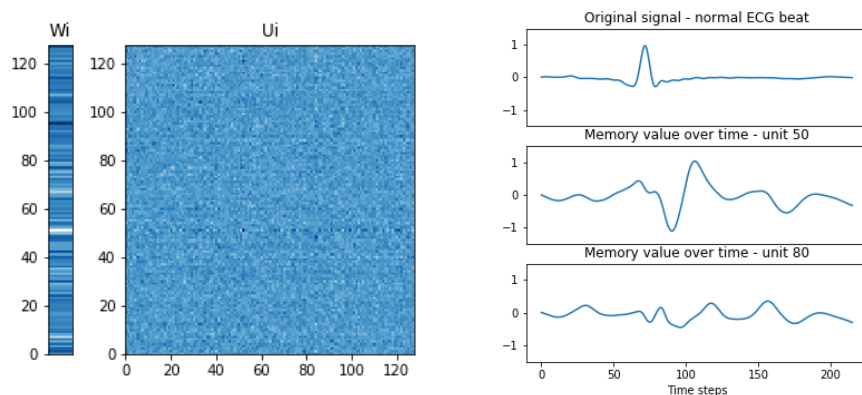


Figure 1: Uninterpretable examples. *Left*: Illustration of an arbitrary set of parameters for an LSTM trained on the MIT-BIH dataset. Numbers indicate different connections for the input weight vector (rectangle) and the hidden layer weight matrix (square). *Right*: The memory values  $c$  for arbitrary units in the LSTM trained on the MIT-BIH data.

It is hard to determine exactly what features LSTMs extract from signals, and it is believed that the models learn to perform complex filter operations on the time series, similar to the deeper layers of CNNs. Some of the hidden units in our analyses display outputs that are roughly similar to wavelet coefficients. In Figure 2 we collate cherry-picked examples of wavelet coefficients and hidden unit outputs from the LSTM models. From the figure, certain hidden units in the LSTM appear to act as approximate wavelet coefficients for extraction of frequency domain features from the signal. Many of the hidden unit outputs also look like combinations of wavelet coefficients. The wavelet transform is a hand-engineered operation that requires expert domain knowledge to perfect and it is difficult to

select the type of wavelet. It could be argued that the LSTMs learn the most suitable wavelet-like coefficients serendipitously. There remain a plethora of other filter operations that could also be compared to the hidden unit outputs in the same manner. Knowing that end-to-end trained LSTM models learn filter-like operations is a potential reassurance to the medical community.

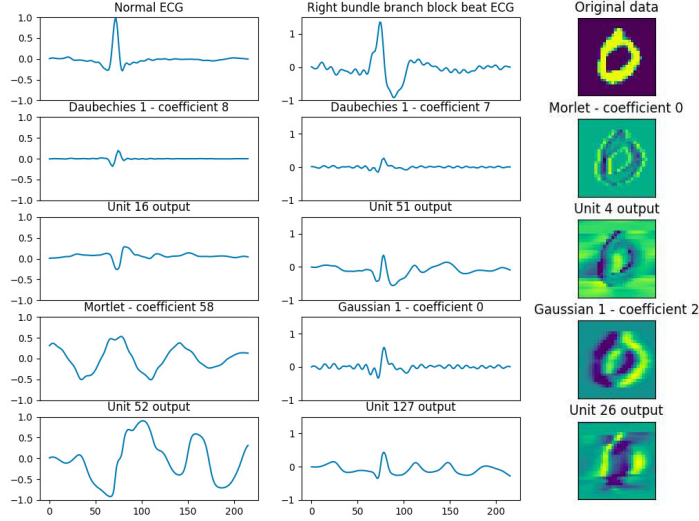


Figure 2: LSTM hidden unit outputs compared to wavelet coefficients. The top of each column is the original sample that was correctly classified using the respective LSTM model. The following two pairs of rows are the cherry-picked pairs of wavelet coefficients and hidden unit outputs that are roughly similar. The type of wavelet coefficient and the specific hidden unit are indicated above each plot. The Daubechies wavelet coefficients are 108 time steps long (instead of 216) because it makes use of the discrete wavelet transform. The wavelet coefficients were computed using the PyWavelets package in Python.

## 5 Visualizing LSTM decisions

Similar to the work by Lanchantin et al. [12], we employ techniques developed in the CNN domain for displaying salient features on the input according to the model. These comprise deriving the inputs with respect to the score of a specific sample, visualizing the optimal input per class [23], and temporal output scores. We also perform, what is according to our knowledge, the first saliency visualization by means of occlusion for LSTMs. The visualization techniques used are discussed in the following sections.

### 5.1 Input feature saliency

Depending on the data, a time series contains a certain amount of noise and a certain number of time steps that are redundant. Hidden Markov Models could be seen as a form of compressing the redundant information – the model switches to a new hidden state when the incoming time steps are no longer redundant [22]. When an LSTM model classifies a signal, knowing the influence that each input has on the output can help us both understand the models and predict where they might fail. The input saliency could indicate what information is considered redundant or noisy by the model. Given a sequence  $X_0$  with  $N$  time steps, and class  $c$ , an LSTM provides a score function  $S_c(X_0)$ . Owing to the score function being highly non-linear, it is difficult to determine the influence of each input of  $X_0$  on  $S_c$ . However, we can approximate  $S_c(X)$  with a linear function in the neighborhood of  $X_0$  by computing the first-order Taylor expansion:

$$S_c(X) \approx \omega^T X + b, \quad (1)$$

where  $\omega$  is the derivative of  $S_c$  with respect to the sequence  $X$  at the point (sequence)  $X_0$ :

$$\omega = \left. \frac{\partial S_c}{\partial X} \right|_{X_0} = \text{saliency map} \quad (2)$$

The resulting saliency indicates which inputs will have the most significant impact on the output. The derivative in Equation 2 is computed with a single step of backpropagation in the LSTM. In Figures 3 and 4, discussed below, we show that this is a poor approximation, and should be implemented with caution.

Another approach to input saliency is by iteratively occluding sections of the input, which we adopted from the CNN application by Zeiler and Fergus [28]. Occlusion of the sequence inputs is performed by replacing the input values by a specific occluding value. For the true class of the sequence  $X$  the class probability, given by the model, is summed for iterative occlusions of sections within  $X$ . The result is a total probability of belonging to the true class per time step, which is then normalized to heat values between 0 and 1. The occlusion technique additionally provides a method for determining intra-dependence of sub-segments in a sequence through the application of different occlusion signals as filters to the original signal. In the MNIST dataset, for example, which has a known structure of 28x28 pixels for each sample, it makes sense to use an occlusion filter that occludes a 5x5 pixel block in the image space. To achieve this, 5 consecutive pixel values are occluded 5 times with 28 time steps between the start of each consecutive set. In the 2D space, this amounts to the same block occlusion technique used for CNNs [28], but the implications are different due to LSTMs being temporal.

In Figures 3 and 4 we juxtapose the different input saliency approaches for the ECG and MNIST data respectively. From the figures, it is evident that derivatives of the input yield the least interpretable representations. For LSTMs deriving the output scores with respect to the input is a poor approximation of saliency. When concurrently perturbing multiple inputs in a time series, the derivatives would vary significantly for different perturbations of the inputs. Occluding sub-segments of a time series provides a better approach for input saliency in our datasets.

Occlusion with zero-valued vectors produces interpretable visualizations, and for the MNIST dataset, this corresponds to masking the digits with the background of the image. Various occlusion values were tested, including the mean and the mode values of each sample, but the values 0 and 0.5 yielded the most interpretable results. Empirically we found that the length of the occluded section is proportional to the temporal dependence length of the model elucidated by the saliency technique. Where the derivatives show the influence each input has, occluding values show the effect of setting sections of the input to a specific value. Consequently occluding inputs to show saliency provide two benefits: (i) determining the impact of expected corruption values or noise on output (such as missing values in vital signs), and (ii) discovering structural input dependencies (with techniques such as block occlusion filters). Specifically, elucidating saliency on medical signals could help doctors understand what is important in complex signals. This could also allow doctors to further investigate dubious LSTM model analysis. Interestingly, using a block occlusion filter with a value of 0.5 on the MNIST data yields the negative of the actual digit. For this 5x5 structural dependency, the model seemingly focuses on the area around the digit (the pixels that should all be zero) to determine what number it is.

Figure 5 illustrates input feature saliency obtained from occluding and deriving multivariate signals in the ICU (left) and NICU (right) datasets. When occluding all the input features concurrently, i.e., setting all the variables in the time series to zero for each occluded section, we obtain the section of the multivariate time series that was the most important for classification (see Figure 5, left). Occluding one input variable at a time provides an indication of the variable (signal) that is most important for classification along with the different sections within each variable’s time series that is salient. For the NICU data the derivatives again yielded uninterpretable results. However, for the ICU data the derivatives yielded a more interpretable saliency, which could be a result of the shorter sequences in the ICU dataset that make the approximation (Equation 2) more suitable. In other words, the approximation could work for shallower networks. More examples of the input feature saliency are illustrated in the supplementary material.

## 5.2 Class mode visualization

In this section, we describe a technique for visualizing the different classes of the models. The method entails optimizing the input with respect to the class score  $S_c$ , whilst keeping the model parameters fixed. More formally, we would like to find an  $L_2$ -regularized input  $X$  that maximizes the score  $S_c$  of the class  $c$ :

$$\arg \max_X S_c(X) - \lambda \|X\|_2^2 \tag{3}$$

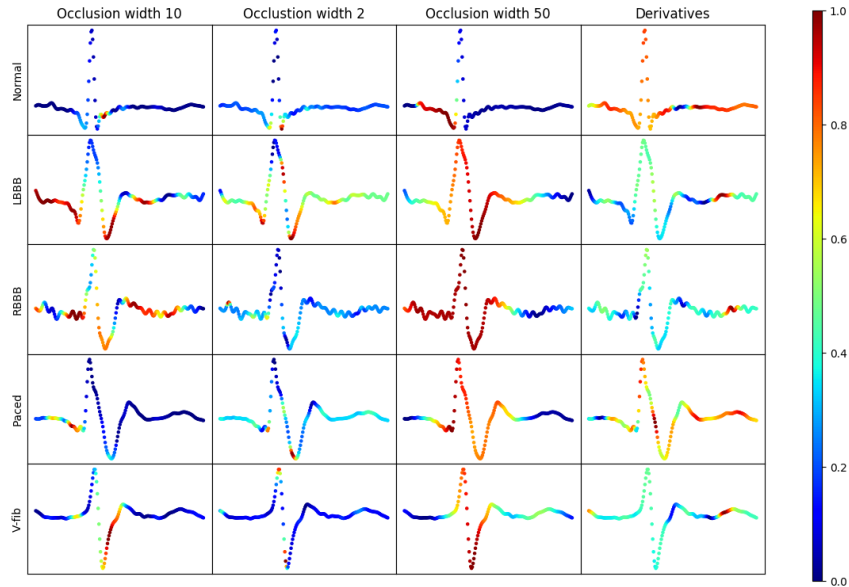


Figure 3: The sample saliencies for the ECG data using different techniques depicted in each column. The occlusion width is the number of time steps that are occluded per instance. All the samples shown have a length of 216 time steps (x-axis) and were correctly classified by the model. The importance of each input step is shown on a scale of 0 to 1, with 1 being the most important. The type of ECG signal is indicated on the left with LBBB – left bundle branch block beat, RBBB – right bundle branch block beat, Paced – paced beat, and V-fib – ventricular fibrillation.

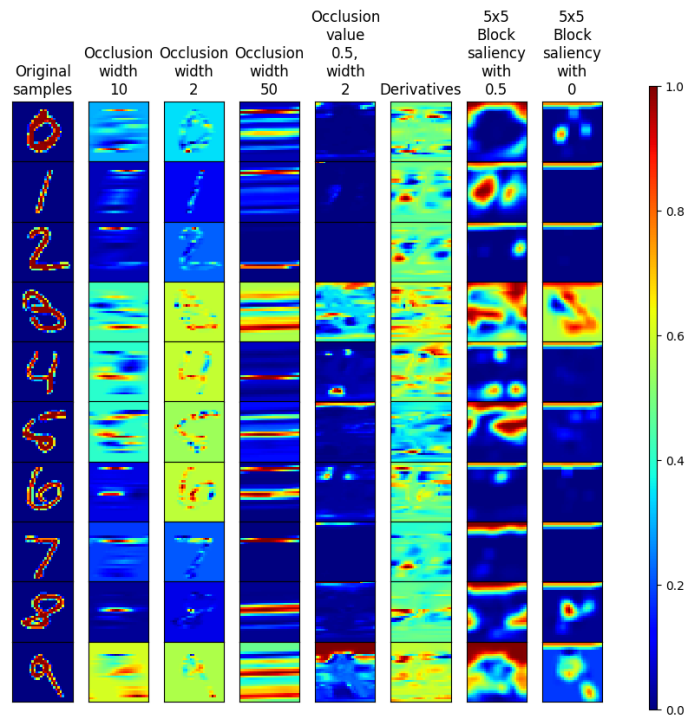


Figure 4: The sample saliencies for arbitrary MNIST samples using different techniques depicted in each column. All the samples shown were correctly classified by the model. The importance of each input step is shown on a scale of 0 to 1, with 1 being the most important. Each row shows the analyses of the same original sample.

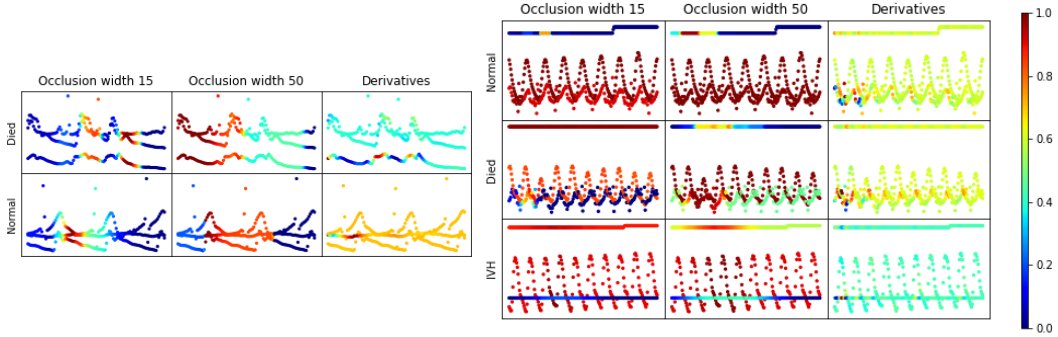


Figure 5: Multivariate input feature saliencies. Y-axis labels indicate the class of the samples. *Left*: Saliency of ICU data inputs occluded concurrently. Signals comprise ECG, blood pressure, and intracranial pressure and are 100 time steps long. *Right*: Saliency of NICU data input signals occluded independently. The signals include ECG, blood pressure, and oxygen saturation and are 216 time steps long.

where  $\lambda$  is a regularization parameter empirically found to be 0.3. We use RMSProp to optimize Equation 3 with respect to the randomly initialized variable  $X$ . We follow the recommendation by Simonyan et al. [23] and explicitly use the unnormalized class score  $S_c$  and not the softmax output of the LSTM.

Figure 6 illustrates the optimum class inputs for this model. Applied to our datasets this method converges to uninterpretable signals. This is most likely a result of the model not exploring all the possible areas of the input space during training, similar to the concerns raised in Nguyen et al. [19] and Szegedy et al. [25]. Effectively, the model can easily be fooled to classify arbitrary noise into some class with absolute confidence. This is a consequence of the model not having seen something similar to the arbitrary noise during training, and it is a known Neural Network optimization problem that is mitigated by Generative Adversarial Networks [5].

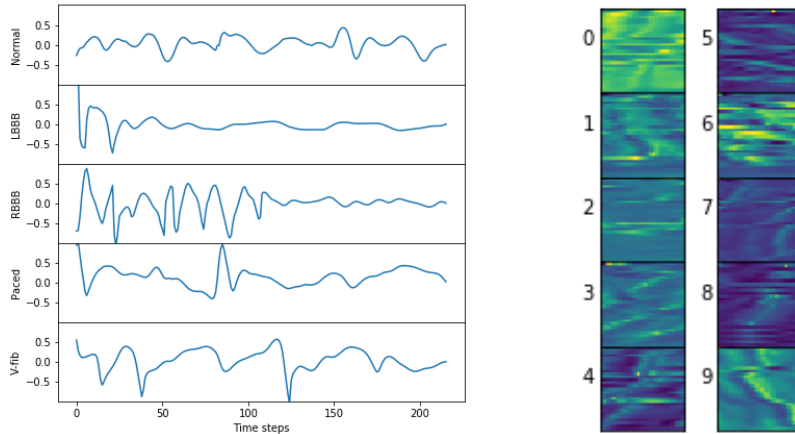


Figure 6: Class mode visualizations. The optimized class modes for the ECG data (left) and the MNIST data (right). Here the input is optimized with respect to each class in order to find the most likely input for each class. The class for each plot is indicated on the left of the image. This technique did not yield interpretable results. See Figure 3 for the meanings of the abbreviations.

### 5.3 Temporal output scores

The final visualization technique illustrates the progression of model decisions over time for a specific time series. This method involves the computation of the classification scores for incrementally longer sections of the time series in order to visualize model decisions at each time step. In other words, for a sequence  $X$  with length  $N$  we classify time steps 1 to  $n$  of the original signal, where  $n$

ranges from 1 to  $N$ . In Figure 7 we illustrate the temporal output scores for the different datasets. The output scores are displayed as either the most probable class given by the model per time step, or the correct class probability (heat) given by the model. This technique allows us to visualize how early the correct classification was made in a sequence, and what other classes were considered. Interestingly, all MNIST samples are classified as a nine, and all the ECG signals are classified as normal for the initial time steps. These initial classifications could be seen as the prior learned by the model.

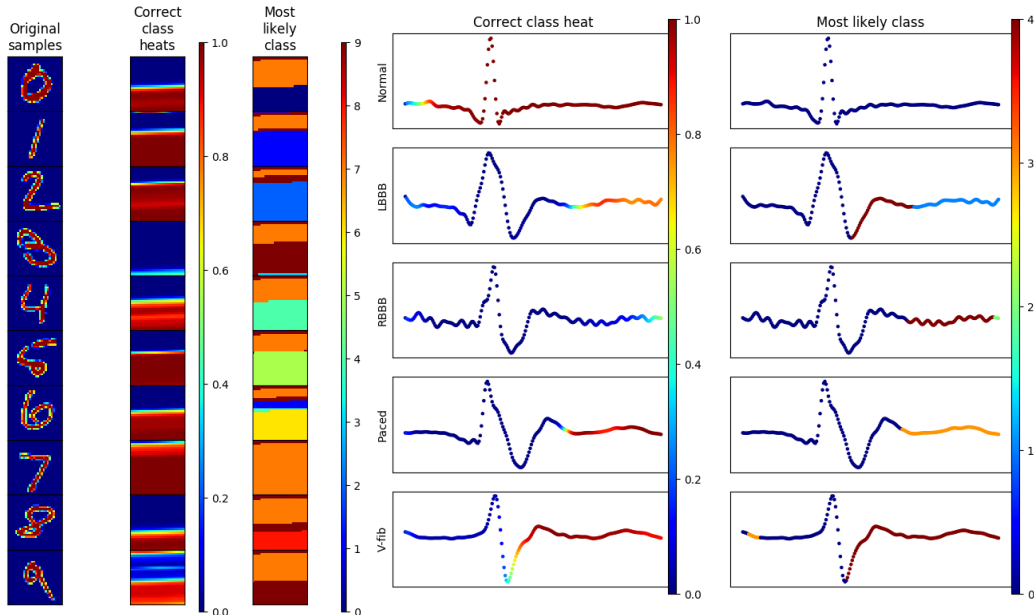


Figure 7: Temporal output scores. *Left*: The temporal output scores for the MNIST dataset. *Right*: The temporal output scores for the ECG dataset. The heat maps show the estimated probability of the sample belonging to the correct class. For the most likely class at each time step, the classes are color-coded as indicated by the color bar to the right of these graphs (classes are zero-indexed). See Figure 3 for the meaning of the abbreviations.

## 6 Conclusion

LSTMs belong to a class of deep neural networks that are particularly difficult to interpret. This study goes some way to improving our understanding of these models by means of a new combination of data and analysis techniques. We draw specific attention to the benefits this holds for augmentation of the medical field with intelligent machine learning diagnostics. The techniques employed in this study can be used by medical practitioners to understand and review LSTM model decisions.

In this study, we showed that the hidden units of LSTMs seem to extract representations from the frequency domain similar to wavelet transformations. We also demonstrated the utility of a new visualization technique for LSTM input saliency – occlusion filters. Analyzing the mechanisms of LSTMs with data different to that used in Karpathy et al. [9] and Lanchantin et al. [12] provided additional insights of LSTMs. Moreover, techniques useful for elucidating LSTM operations with regard to specific datasets are not a panacea for other domains. Unlike CNNs, LSTMs are applied to various types of time series, and analyzing the LSTMs on all these different types is vital.

## References

[1] Abadi, M., Agarwal, A., Barham, P., Brevdo, E., Chen, Z., Citro, C., S. Corrado, G., Davis, A., Dean, J., Devin, M., Ghemawat, S., Goodfellow, I., Harp, A., Irving, G., Isard, M., Jia, Y., Jozefowicz, R., Kaiser, L., Kudlur, M., Levenberg, J., Mané, D., Monga, R., Moore, S., Murray, D., Olah, C., Schuster, M., Shlens, J., Steiner, B., Sutskever, I., Talwar, K., Tucker, P., Vanhoucke, V.,

- Vasudevan, V., Viégas, F., Vinyals, O., Warden, P., Wattenberg, M., Wicke, M., Yu, Y., and Zheng, X. (2015). TensorFlow: Large-Scale Machine Learning on Heterogeneous Systems. Software available from tensorflow.org.
- [2] Cooijmans, T., Ballas, N., Laurent, C., Gülçehre, Ç., and Courville, A. (2016). Recurrent batch normalization. *arXiv preprint arXiv:1603.09025*.
- [3] Gal, Y. (2016). *Uncertainty in Deep Learning*. PhD thesis, PhD thesis, University of Cambridge.
- [4] Goldberger, A. L., Amaral, L. A. N., Glass, L., Hausdorff, J. M., Ivanov, P. C., Mark, R. G., Mietus, J. E., Moody, G. B., Peng, C.-K., and Stanley, H. E. (2000). PhysioBank, PhysioToolkit, and PhysioNet Components of a New Research Resource for Complex Physiologic Signals. *Circulation*, 101(23):e215–e220.
- [5] Goodfellow, I., Pouget-Abadie, J., Mirza, M., Xu, B., Warde-Farley, D., Ozair, S., Courville, A., and Bengio, Y. (2014). Generative Adversarial Nets. In Ghahramani, Z., Welling, M., Cortes, C., Lawrence, N. D., and Weinberger, K. Q., editors, *Advances in Neural Information Processing Systems 27*, pages 2672–2680. Curran Associates, Inc.
- [6] Graves, A. (2013). Generating Sequences With Recurrent Neural Networks. *arXiv:1308.0850 [cs]*.
- [7] Hochreiter, S. and Schmidhuber, J. (1997). Long Short-Term Memory. *Neural Computation*, 9(8):1735–1780.
- [8] Jiang, X. and Adeli, H. (2005). Dynamic Wavelet Neural Network Model for Traffic Flow Forecasting. *Journal of Transportation Engineering*, 131(10):771–779.
- [9] Karpathy, A., Johnson, J., and Fei-Fei, L. (2015). Visualizing and Understanding Recurrent Networks. *arXiv:1506.02078 [cs]*.
- [10] Kingma, D. and Ba, J. (2014). Adam: A Method for Stochastic Optimization. *arXiv:1412.6980 [cs]*.
- [11] Krizhevsky, A., Sutskever, I., and Hinton, G. E. (2012). ImageNet Classification with Deep Convolutional Neural Networks. In Pereira, F., Burges, C. J. C., Bottou, L., and Weinberger, K. Q., editors, *Advances in Neural Information Processing Systems 25*, pages 1097–1105. Curran Associates, Inc.
- [12] Lanchantin, J., Singh, R., Wang, B., and Qi, Y. (2016). Deep Motif Dashboard: Visualizing and Understanding Genomic Sequences Using Deep Neural Networks. *arXiv:1608.03644 [cs]*.
- [13] LeCun, Y., Cortes, C., and Burges, C. J. (1998). The mnist database of handwritten digits.
- [14] Li, J., Chen, X., Hovy, E., and Jurafsky, D. (2015). Visualizing and Understanding Neural Models in NLP. *arXiv:1506.01066 [cs]*.
- [15] Li, M., Zhang, M., Luo, X., and Yang, J. (2016). Combined long short-term memory based network employing wavelet coefficients for MI-EEG recognition. In *2016 IEEE International Conference on Mechatronics and Automation*, pages 1971–1976.
- [16] Lipton, Z. C., Berkowitz, J., and Elkan, C. (2015a). A Critical Review of Recurrent Neural Networks for Sequence Learning. *arXiv:1506.00019 [cs]*.
- [17] Lipton, Z. C., Kale, D. C., Elkan, C., and Wetzell, R. (2015b). Learning to Diagnose with LSTM Recurrent Neural Networks. *arXiv:1511.03677 [cs]*.
- [18] Moody, G. B. and Mark, R. G. (2001). The impact of the mit-bih arrhythmia database. *IEEE Engineering in Medicine and Biology Magazine*, 20(3):45–50.
- [19] Nguyen, A., Yosinski, J., and Clune, J. (2015). Deep Neural Networks Are Easily Fooled: High Confidence Predictions for Unrecognizable Images. pages 427–436.

- [20] Oresko, J. J., Jin, Z., Cheng, J., Huang, S., Sun, Y., Duschl, H., and Cheng, A. C. (2010). A Wearable Smartphone-Based Platform for Real-Time Cardiovascular Disease Detection Via Electrocardiogram Processing. *IEEE Transactions on Information Technology in Biomedicine*, 14(3):734–740.
- [21] Potes, C., Parvaneh, S., Rahman, A., and Conroy, B. (2016). Ensemble of Feature-based and Deep learning-based Classifiers for Detection of Abnormal Heart Sounds.
- [22] Rabiner, L. and Juang, B. (1986). An introduction to hidden Markov models. *IEEE ASSP Magazine*, 3(1):4–16.
- [23] Simonyan, K., Vedaldi, A., and Zisserman, A. (2013). Deep Inside Convolutional Networks: Visualising Image Classification Models and Saliency Maps. *arXiv:1312.6034 [cs]*.
- [24] Sutskever, I., Vinyals, O., and Le, Q. V. (2014). Sequence to sequence learning with neural networks. In *Advances in neural information processing systems*, pages 3104–3112.
- [25] Szegedy, C., Zaremba, W., Sutskever, I., Bruna, J., Erhan, D., Goodfellow, I., and Fergus, R. (2013). Intriguing properties of neural networks. *arXiv preprint arXiv:1312.6199*.
- [26] Temko, A., Thomas, E., Marnane, W., Lightbody, G., and Boylan, G. (2011). EEG-based neonatal seizure detection with Support Vector Machines. *Clinical Neurophysiology*, 122(3):464–473.
- [27] Zabihi, M., Rad, A. B., Kiranyaz, S., Gabbouj, M., and Katsaggelos, A. K. (2016). Heart Sound Anomaly and Quality Detection using Ensemble of Neural Networks without Segmentation.
- [28] Zeiler, M. D. and Fergus, R. (2014). Visualizing and Understanding Convolutional Networks. In *Computer Vision – ECCV 2014*, pages 818–833. Springer, Cham.
- [29] Zhang, S., Wu, Y., Che, T., Lin, Z., Memisevic, R., Salakhutdinov, R. R., and Bengio, Y. (2016). Architectural complexity measures of recurrent neural networks. In *Advances in Neural Information Processing Systems*, pages 1822–1830.
- [30] Zhou, J. and Troyanskaya, O. G. (2015). Predicting effects of noncoding variants with deep learning-based sequence model. *Nature methods*, 12(10):931–934.